Angewandte Chemie
Eine Zeitschrift der Gesellschaft Deutscher Chemiker

Supporting Information

Noncovalent Functionalization and Charge Transfer in Antimonene

Gonzalo Abellán, Pablo Ares, Stefan Wild, Edurne Nuin, Christian Neiss, David Rodriguez-San Miguel, Pilar Segovia, Carlos Gibaja, Enrique G. Michel, Andreas Görling, Frank Hauke, Julio Gómez-Herrero, Andreas Hirsch, and Félix Zamora**

anie_201702983_sm_miscellaneous_information.pdf

Supporting Information

1. Materials and Methods

General. Tert-butyl bromoacetate was provided from abcr. Perylene-3,4,9,10-tetracarboxylic dianhydride (PTCDA), tetracyanoquinodimethane (TCNQ), N,N-Diisopropylethylamine (DIPEA), 1,4-diaminobutane, tetrahydrofurane, 2-propanol and acetonitrile (ACN, HPLC grade) were purchased from Aldrich. Toluene (HPLC grade) was from VWR. NMR spectra were recorded on a Jeol EX 400 (400 MHz) and chemical shifts are given in parts per million (ppm) and referenced to the residual solvent.

Antimonene mechanical exfoliation: bulk, commercially available antimony material (99.9999%, Smart Elements) was used. Preparation of isolated few-layer antimonene flakes was carried out using the mechanical exfoliation technique outlined in ref.[1]. Thin antimonene flakes were transferred to Si (with 300 nm of SiO_2 capping layer) substrates and first imaged using optical microscopy.

On-surface non-covalent functionalization with perylene diimide (PDI): The exfoliated few-layer antimonene samples were functionalized by drop casting PDI molecules dissolved in THF ($c = 10^{-5}$ M) onto the different wafers. Residual PDI was removed by drop casting isopropanol during spin coating of the samples.

Liquid phase exfoliation procedure and characterization:

LPE in IPA: 10 mg of powdered antimony submitted to ball milling treatment were put on a 20 mL vial with 10 mL of 2-propanol. The mixture was sonicated for 40 min. at 400 W and 24 kHz delivering the ultrasound power in pulses 0.5 s long every 1 s. Then, a 10^{-5} M PDI solution was added and stirred during 2 days. For the AFM and Raman analysis 20 μL of the suspension were casted or spin coated on a SiO_2 surface and allowed to dry.

LPE in THF under inert conditions: Antimonene was exfoliated under inert conditions by sonication in an argon-filled glovebox (O_2<0.1 p.p.m.; H_2O<0.1 p.p.m.) in pump-freeze deoxygenated and dry THF (0.01 $g \cdot l^{-1}$ Sb, 10ml THF, tapered tip Bandelin Sonoplus 3100, 25% amplitude, 4 h, pulse 2 s on, 2 s off). The resultant dispersions were transferred into sealed cuvettes. All solvent transfer was carried out in the glovebox.

Sonicator device: Sonication was performed using a Hielscher UP400S ultrasonic processor equipped with a 3 mm sonotrode.

Centrifugation: Centrifugation was carried out in a MPW-350R centrifuge using 2 mL Eppendorfs.

Atomic Absorption Spectrometry: Antimony determination was carried out by flame atomic absorption spectrometry using a ContrAA 700 high-resolution atomic absorption spectrometer (Analitik Jena, Germany). The main line for antimony at 217.5815 nm was employed for all the analysis. The atomization was performed using an air acetylene flame with an acetylene flow rate of 60 $L \cdot h^{-1}$ and at a 6.0 mm burner height. The aspiration rate was fixed at 5 $mL \cdot min^{-1}$. All measurements were carried out in triplicate.
Turbidimeter: Measurements were carried out using a HI-88713 Bench Top Turbidity Meter Hanna Instruments.
Absorption spectroscopy: Optical extinction and absorbance was measured on a Perkin Elmer Lambda 1050 spectrometer in extinction, in quartz cuvettes with a path length of 0.4 cm.
Emission spectroscopy: Fluorescence was acquired on a Horiba Scientific Fluorolog-3 system equipped with 450 W Xe halogen lamp, double monochromator in excitation (grating 600 lines/mm blazed at 500 nm) and emission (grating 1200 lines/mm blazed at 500 nm) and a PMT detector using quartz cuvettes with a path length of 1.0 cm. Spectra were obtained at room temperature.
Atomic force microscopy (AFM) imaging: AFM measurements were carried out using a Cervantes Fullmode AFM from Nanotec Electronica S.L. WSxM software (www.wsxmsolutions.com) was employed both for data acquisition and image processing.[2,3] Topographical images were acquired in a non-contact imaging mode to ensure that the tip would not deform the flakes. This is particularly relevant after the self-assembly of the PDI molecules on the antimonene surface. PPP-FM probes from Nanosensors™ (www.nanosensors.com) were employed. They have a resonant frequency of 75 kHz in air and a nominal stiffness of 2.8 $N\ m^{-1}$. The tip has a radius of curvature < 10 nm.

Optical microscopy imaging: optical micrographs were acquired in a Zeiss Axio Imager.A2m optical microscope using white light illumination at normal incidence with a 100× objective.

Surface preparation: SiO_2 surfaces were sonicated for 15 min. in acetone and 15 min. in 2-propanol and then dried under an argon flow.

Scanning X-ray Photoelectron Microscopy (SPEM): experiments were performed at the ESCAmicroscopy beamline,[4] receiving synchrotron light from the Elettra storage ring in Trieste (Italy). The monochromatic x-ray beam is focused on the sample using a Fresnel zone plate combined with an order-selecting aperture. The sample-illuminated

area has a diameter around 150 nm and is raster scanned with respect to the microprobe. Photoelectrons are collected with a Specs-Phoibos 100 hemispherical analyzer and detected using a 48-chanel electron detector.[5] The electron analyzer axis is fixed at 30º with respect to the surface normal, in order to enhance the surface sensitivity of the instrument.

SPEM can be performed in imaging spectromicroscopy and micro spot spectroscopic modes. The imaging spectromicroscopy mode probes the lateral distribution of elements by collecting photoelectrons with a selected kinetic energy window, while scanning the specimen with respect to the microprobe. The spatial variation in the contrast of the images reflects the variation of the photoelectron yield, which is a measure of the local concentration of the corresponding chemical species. The micro spot mode is identical to the conventional X-ray Photoelectron Spectroscopy (XPS) technique. In this mode, energy distribution curves are measured from the illuminated local micro spot area. Spatially resolved photoemission spectra of selected regions and chemical maps were acquired in this work with 0.2 eV energy resolution by using 652.3 eV photon energy.

Scanning Raman Microscopy (SRM): Raman studies were acquired on a LabRam HR Evolution confocal Raman microscope (Horiba) equipped with an automated XYZ table using 0.80 NA objectives. Throughout all measurements, an excitation wavelength of 532 nm with an acquisition time of 2 s and a laser intensity of 5 % (power) was used. The grating was selected to be 1800 grooves/mm. The step size in conducted Raman mappings was chosen to be 1 µm.

For the wavelength-dependent experiments, laser excitations of 532 nm, 633 nm and 785 nm were used. The step sizes in the Raman mappings were in the 0.5–1 µm range depending on the experiments. Data processing was performed using Lab Spec 5 as evaluation software.

Temperature-dependent Raman Spectroscopy: Temperature-depending Raman measurements were performed in a Linkam stage THMS 600, equipped with a liquid nitrogen pump TMS94 for temperature stabilization under a constant flow of nitrogen. Raman spectroscopic characterization was carried out on a Horiba LabRAM Aramis confocal Raman microscope (λ_{exc}=532 nm) with a laser spot size of *ca*. 1 µm (Olympus LMPlanFl 100., NA 0.80). The incident laser power was kept as low as possible to avoid structural sample damage: 1.35 mW. Spectra were obtained with a CCD array at −70 °C—grating: 600 grooves per mm. Sample movement was carried out by an

automated XY-scanning table. The measurements were carried out on Si/SiO_2 (300 nm oxide layer) and gold substrates with a heating rate of 10 K min^{-1}.

Computational details of DFT calculations

All calculations were done adopting a plane wave basis set within the PAW approach using the Vienna ab-inito Simulation Package (VASP 5.4).[6–10]

For geometry optimizations, we applied the exchange-correlation density functional according to Perdew, Becke and Ernzerhof[11] (PBE) in connection with the Grimme D3 dispersion correction[12,13] (without Becke-Johnson damping) to properly account for van-der-Waals interactions. Most of the geometry optimizations were carried out using the "Gadget" driver by Bučko et al.[14] and were considered converged when all residual force components were smaller than 0.01 eV/Å. The plane wave cut-off energy was for structures containing only Sb atoms 250 eV, only P atoms 300 eV and in all other cases 450 eV. A Methfessel-Paxton smearing of first order with σ=0.05 eV was employed.[15] Bulk structures were optimized allowing for cell relaxation, for mono- and double layers of Sb (P) only the cell volume was fixed during optimization. For the later, a slab approach with at least 15 Å between the slabs was adopted. In case of the PDI functionalized models the cell parameters were kept fixed to those of the optimized "naked" layers. The PDI model was placed on a 6 x 5 super cell in case of BP, and on a 5 x 5 supercell in case of Sb. k-point sampling was done using Monkhorst-Pack meshes,[16] shifted to include the Γ point, if necessary. For further details, see supplementary Tables 1–3.

Final energies were evaluated at the thus obtained geometries applying the HSE06 exchange-correlation functional[17] (which provides more realistic band gaps than PBE), and the tetrahedron method including Blöchl corrections for interpolation between the k-points was used;[18] the plane wave cut-off energy was 450 eV. The remaining setup was as for the geometry optimizations.

2. Synthesis of the perylene bisimide (PDI) derivative

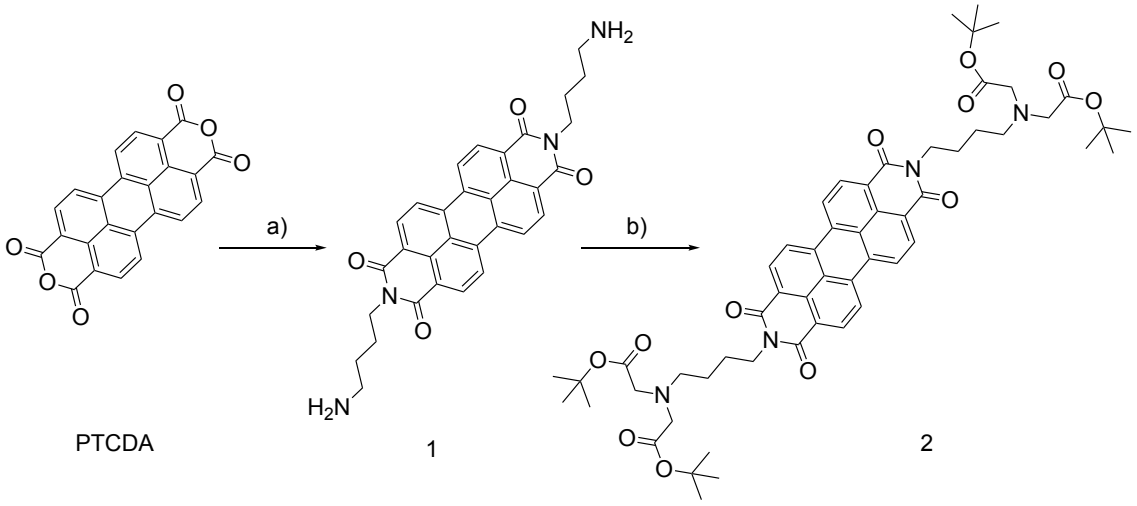

Synthesis of 2: Reagents and conditions: a) Toluene, 1,4-diaminobutane, 118 ºC, 4 h. b) ACN, DIPEA, tert-butyl bromoacetate, 60 ºC, 24 h.

The PDI derivative was synthesized according to Marcia et *al*.[19] Briefly, to a solution of PTCDA (4.1 g, 10.2 mmol, 1.0 eq) in toluene (100 mL), 1,4-diaminobutane (3.6 g, 40.8 mmol, 4.0 eq) was added. After stirring at 118 ºC for 4 h, the reaction mixture was cooled down and filtered, to get a crude, which was washed with toluene and dried under vacuum. Afterwards, the crude solid was re-suspended in KOH 5M (80 mL) and stirred at room temperature for another 15 h. After this time, the suspension was filtered, and the product was washed with water and dried overnight under vacuum to give **1** (4.8 g, 87.5 %) as a red-brownish solid, which is ready to be used in the next step. Subsequently, to a solution of PDI precursor **1** (4.8 g, 8.9 mmol, 1.0 eq) in ACN (255 mL), DIPEA (15.5 mL, 89.2 mmol, 10.0 eq) and tert-butyl bromoacetate (13.9 g, 71.4 mmol, 8.0 eq) were added, and the solution was stirred at 60 ˚C for 24 h. Once the reaction mixture was cooled down to room temperature, the precipitate was filtered and rinsed with water and ACN and dried overnight under vacuum. Finally, to a solution of the solid residue in $CHCl_3$ was added with stirring *n*-hexane, which resulted in the formation of a precipitate. The precipitate was filtered, washed with *n*-hexane to get **2** (4.0 g, 45.3 %) as red solid.

^{1}H NMR (400 MHz, $CDCl_3$, 25 °C): δ 1.44 (s, 36H), 1.63 (quintuplet, J = 7.0 Hz, 4H), 1.79 (quintuplet, J = 7.5 Hz, 4H), 2.77 (t, J = 7.6 Hz, 4H), 3.44 (s, 8H), 4.21 (t, J = 7.4 Hz, 4H), 8.33 (d, J = 8.0 Hz, 4H), 8.48 (d, J = 8.0 Hz, 4H) ppm.^{13}C NMR (100 MHz, $CDCl_3$, 25 °C): δ 25.54, 25.64, 28.05, 40.27, 53.86, 55.73, 80.73, 122.47, 122.85, 125.39, 128.55, 130.62, 133.58, 162.76, 170.77 ppm.

Characterization of 2

^{1}H NMR of 2

(400 MHz,$CDCl_3$)

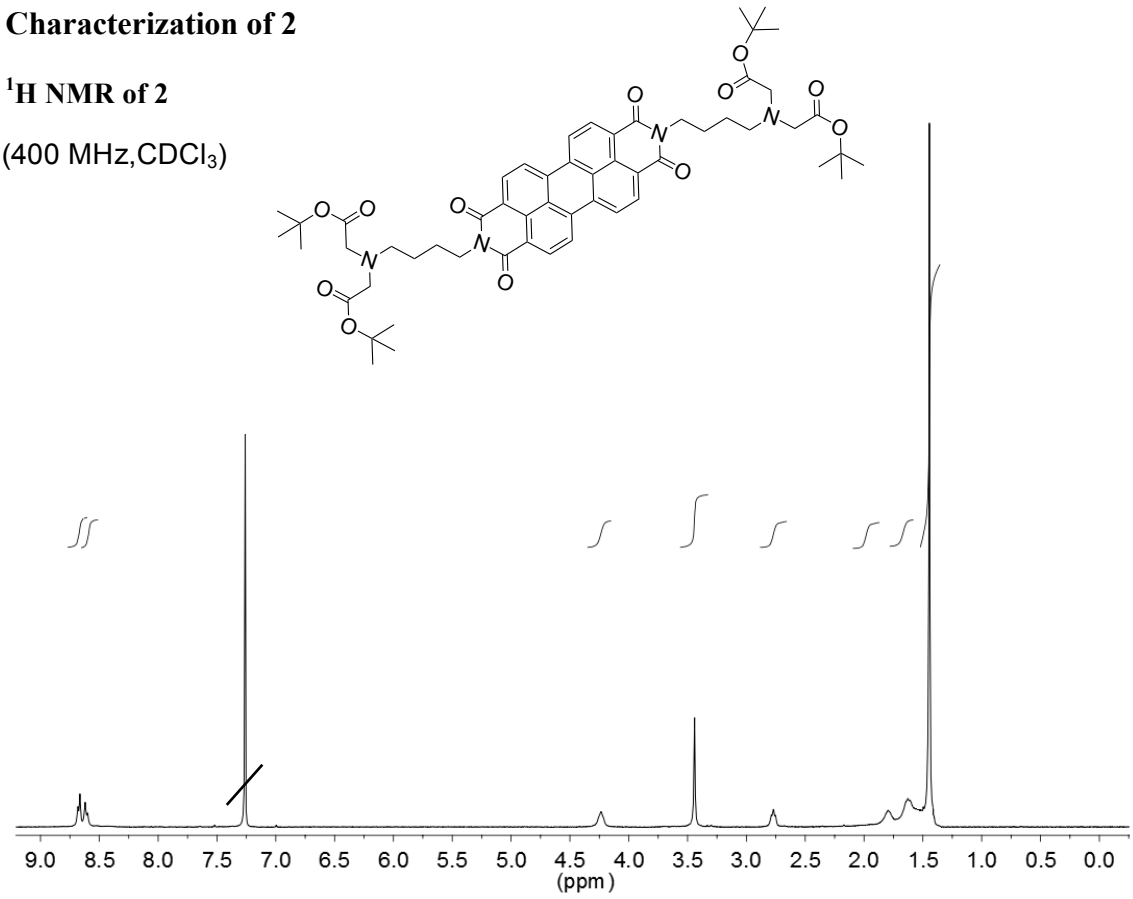

^{13}C NMR of 2

(100 MHz, $CDCl_3$)

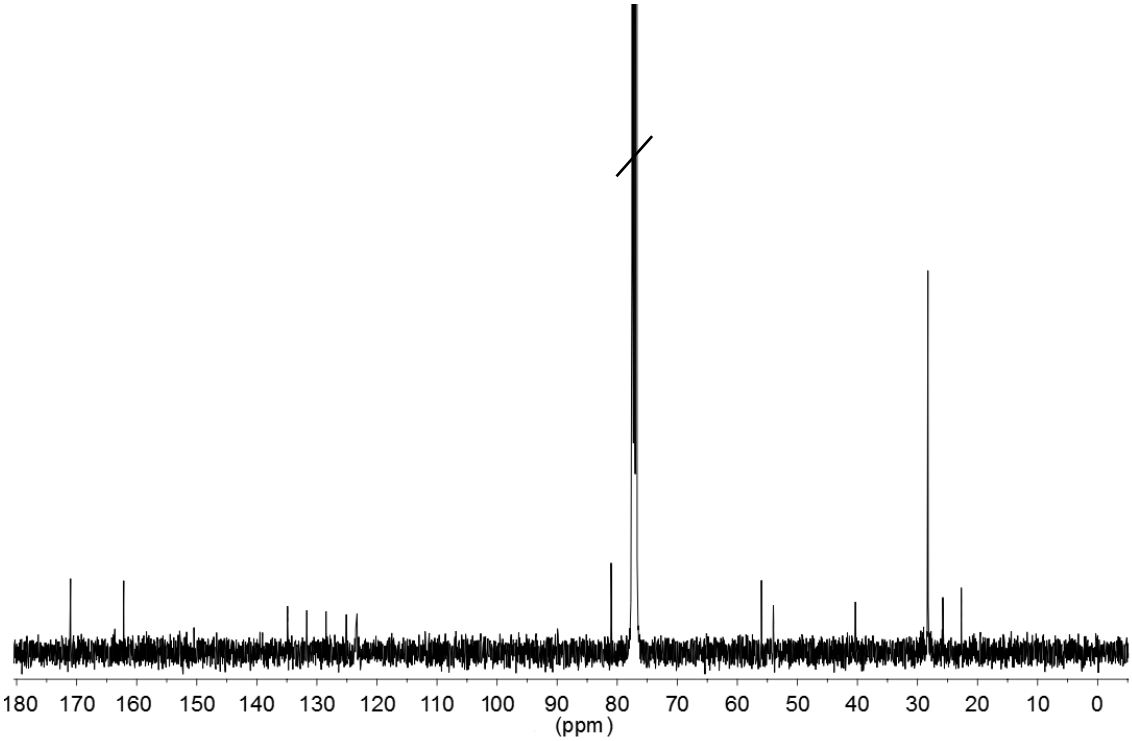

Absorption and emission spectra

Absorption spectrum (solid line) of PDI (1.10^{-5} M in THF, l = 10 mm) and its overlaid fluorescence spectrum (λ_{ex} = 455 nm) (dotted line).

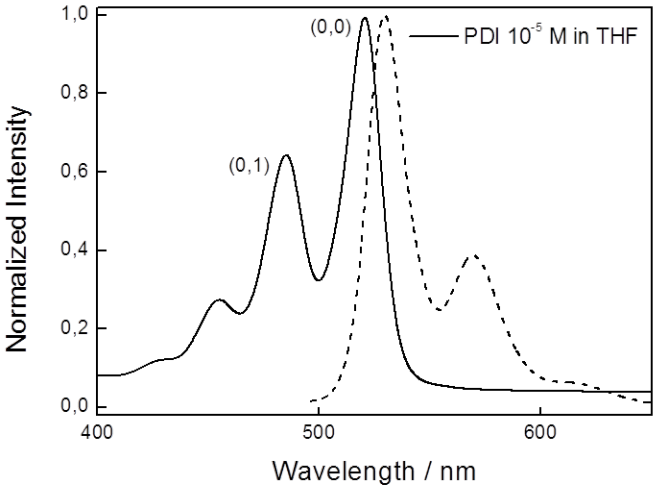

3. AFM imaging of different few-layer antimonene flakes

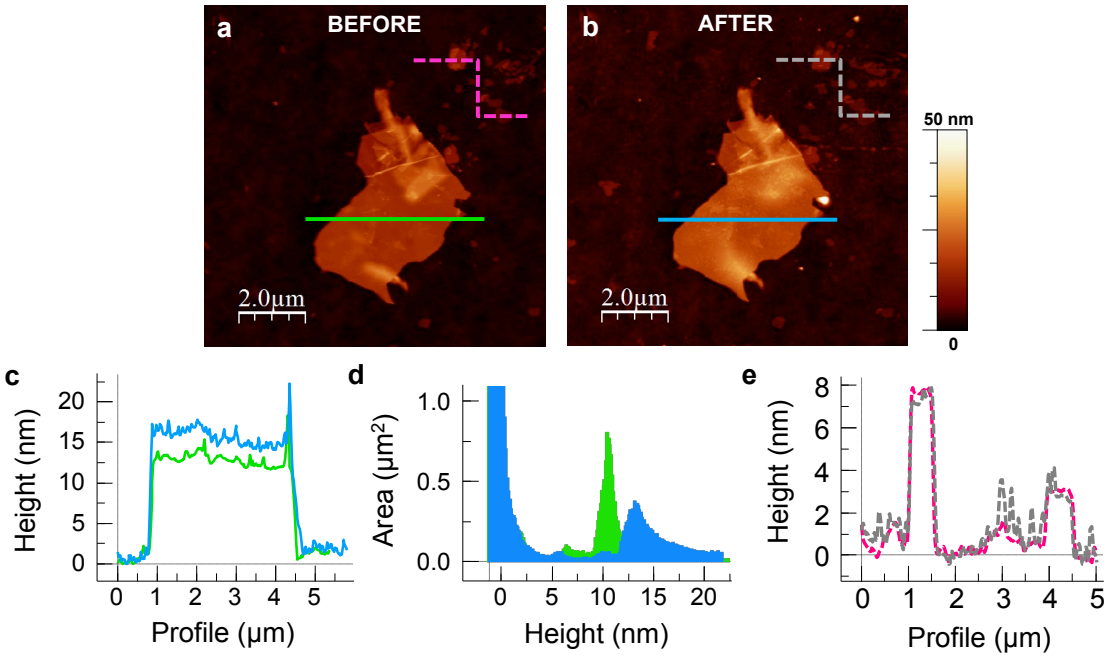

Figure S1. a) AFM image of a few-layer antimonene flake as deposited. b) AFM image of the same flake after the functionalization with PDI molecules. c) Representative profiles, corresponding to the solid lines in the images. d) Height histograms of the flake before (green) and after functionalization (blue), showing an average thickness increase of 2.7 nm. For the sake of clarity, the substrate peak has been cut to 1.1 μm^2. e) Profiles along the dashed lines in the images, corresponding to debris present on the substrate. There is no height change, confirming the exclusive self-assembly of the PDI on the antimonene flakes.

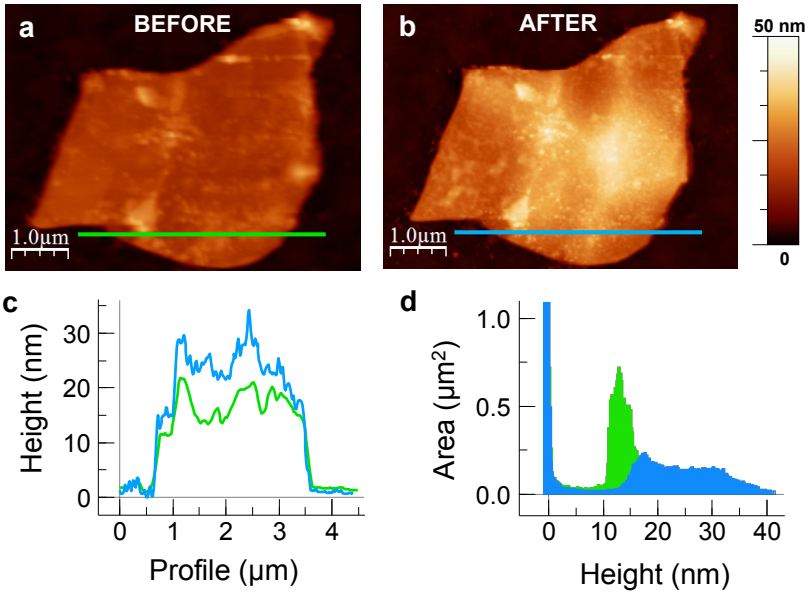

Figure S2. a) AFM image of a few-layer antimonene flake as deposited. b) AFM image of the same flake after the functionalization with PDI molecules. c) Representative profiles, corresponding to the lines in the images. d) Height histograms of the flake before (green) and after functionalization (blue), showing an average thickness increase of 4.5 nm. For the sake of clarity, the substrate peak has been cut to 1.1 μm^2.

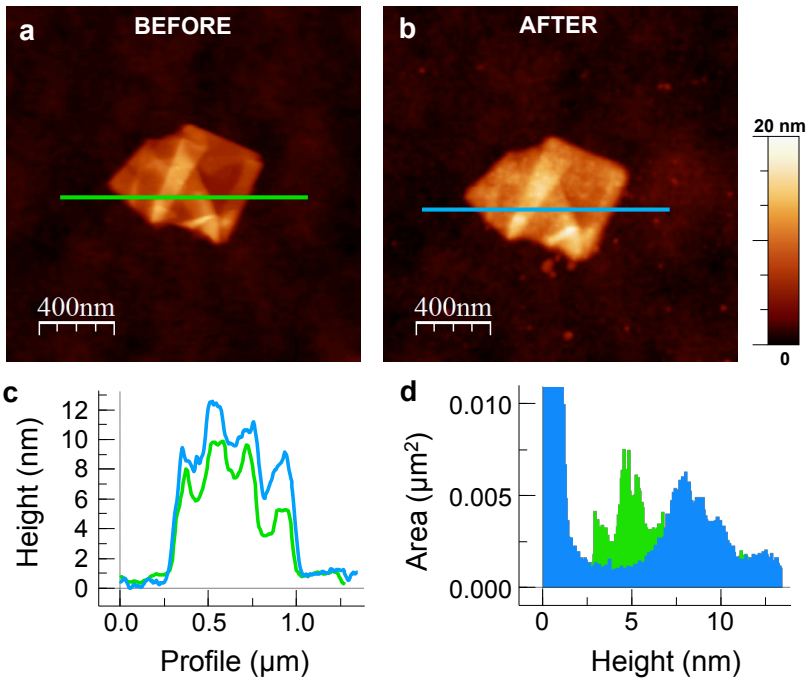

Figure S3. a) AFM image of a few-layer antimonene flake as deposited. b) AFM image of the same flake after the functionalization with PDI molecules. c) Representative profiles, corresponding to the lines in the images. d) Height histograms of the flake before (green) and after functionalization (blue), showing an average thickness increase of 3.1 nm. For the sake of clarity, the substrate peak has been cut to 0.011 μm^2.

4. Absence of correlation between flake thickness and organic covering

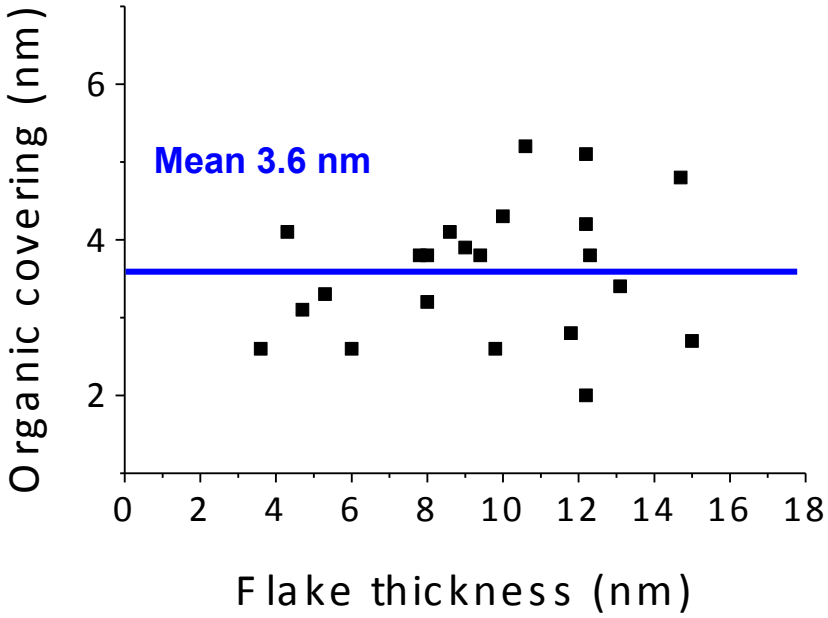

Figure S4. Organic covering *vs.* flake thickness. Data obtained from the comparison of the thicknesses before and after self-assembly of the PDI molecules on the different terraces of all the studied flakes. The average PDI coverage is 3.6 nm. No correlation between flake thickness and organic covering is observed.

5. Optical microscopy

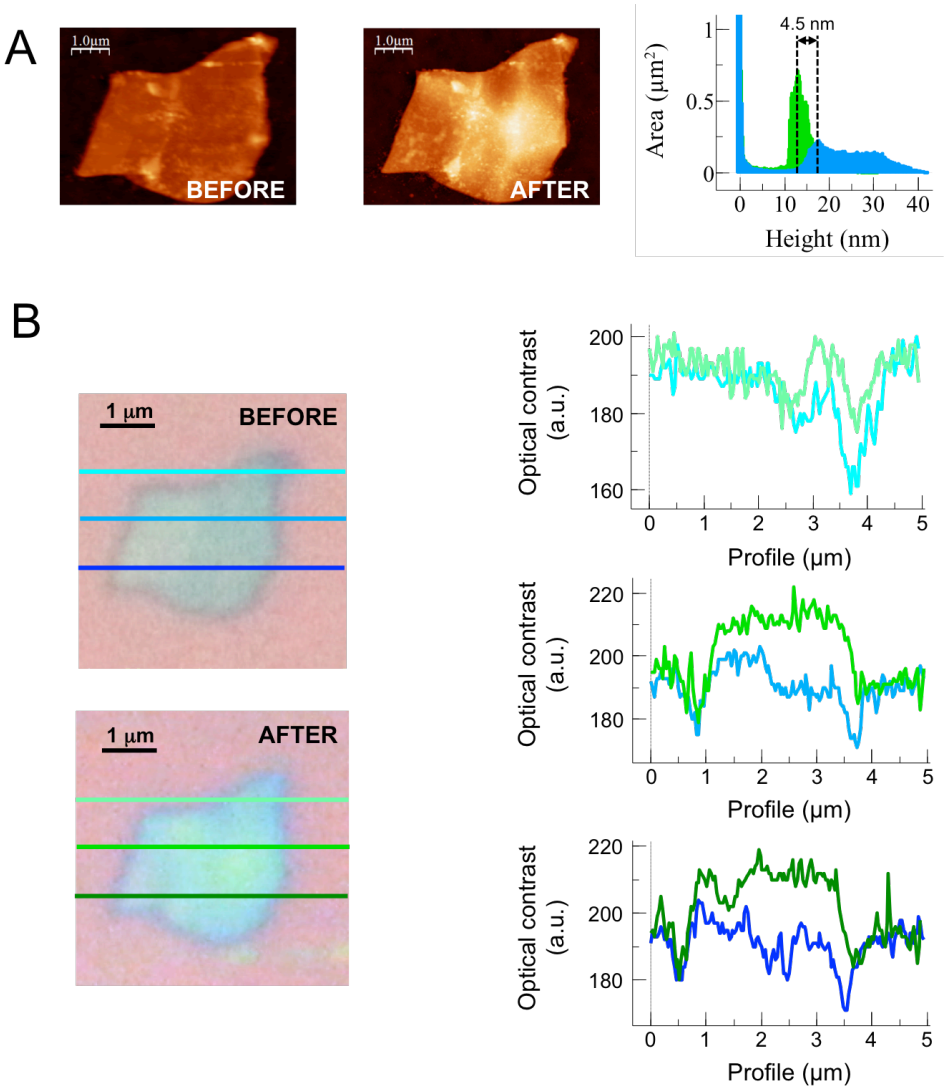

Figure S5. a) Left: AFM images of a few-layer antimonene flake as deposited and after the functionalization with PDI molecules. Right: Height histograms of the flake before (green) and after functionalization (blue), showing an average thickness increase of 4.5 nm. b) Left: different optical images acquired using white light and the corresponding measured optical contrast. Solid lines represent the different analysed profiles.

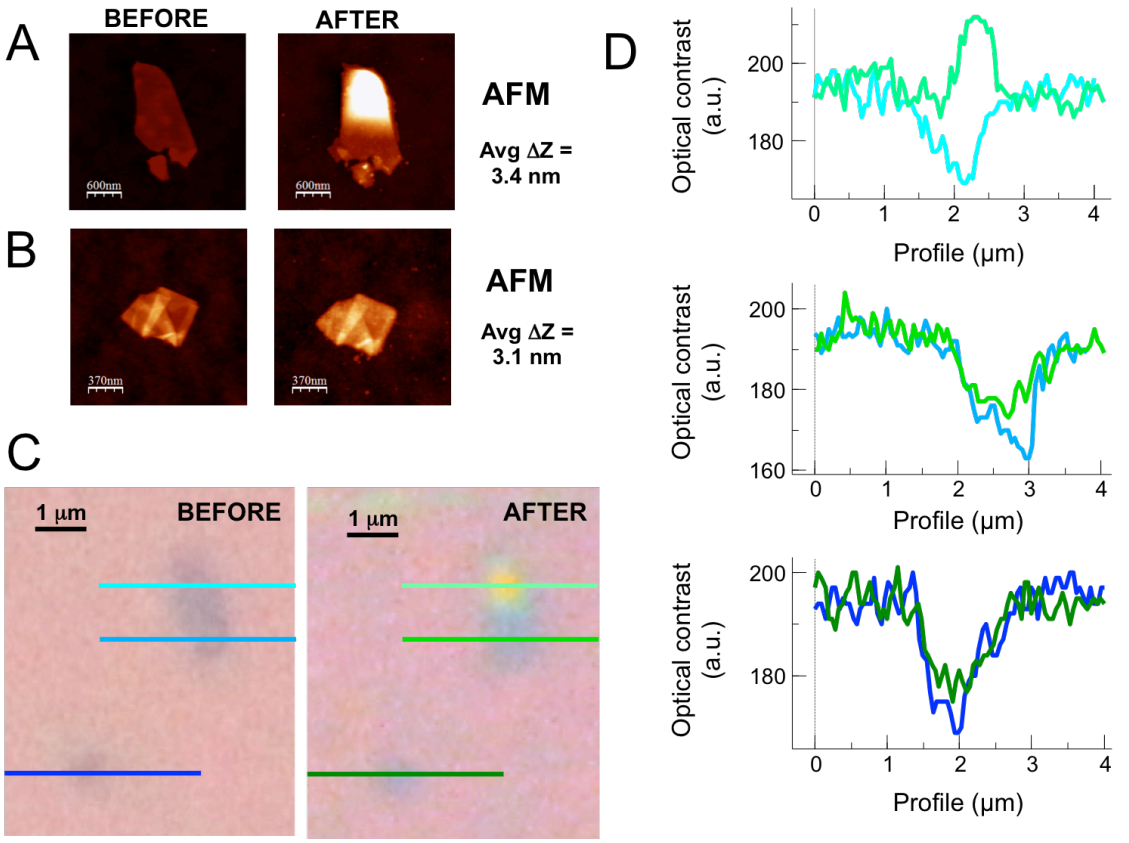

Figure S6. a) and b) AFM images of few-layer antimonene flakes with minimum thicknesses of *ca*. 3 and 5 nm as deposited and after the functionalization with PDI molecules showing a PDI organic thickness of 3.4 and 3.1 nm, respectively. c) Different optical images acquired using white light and d) the corresponding measured optical contrast. Solid lines represent the different analysed profiles.

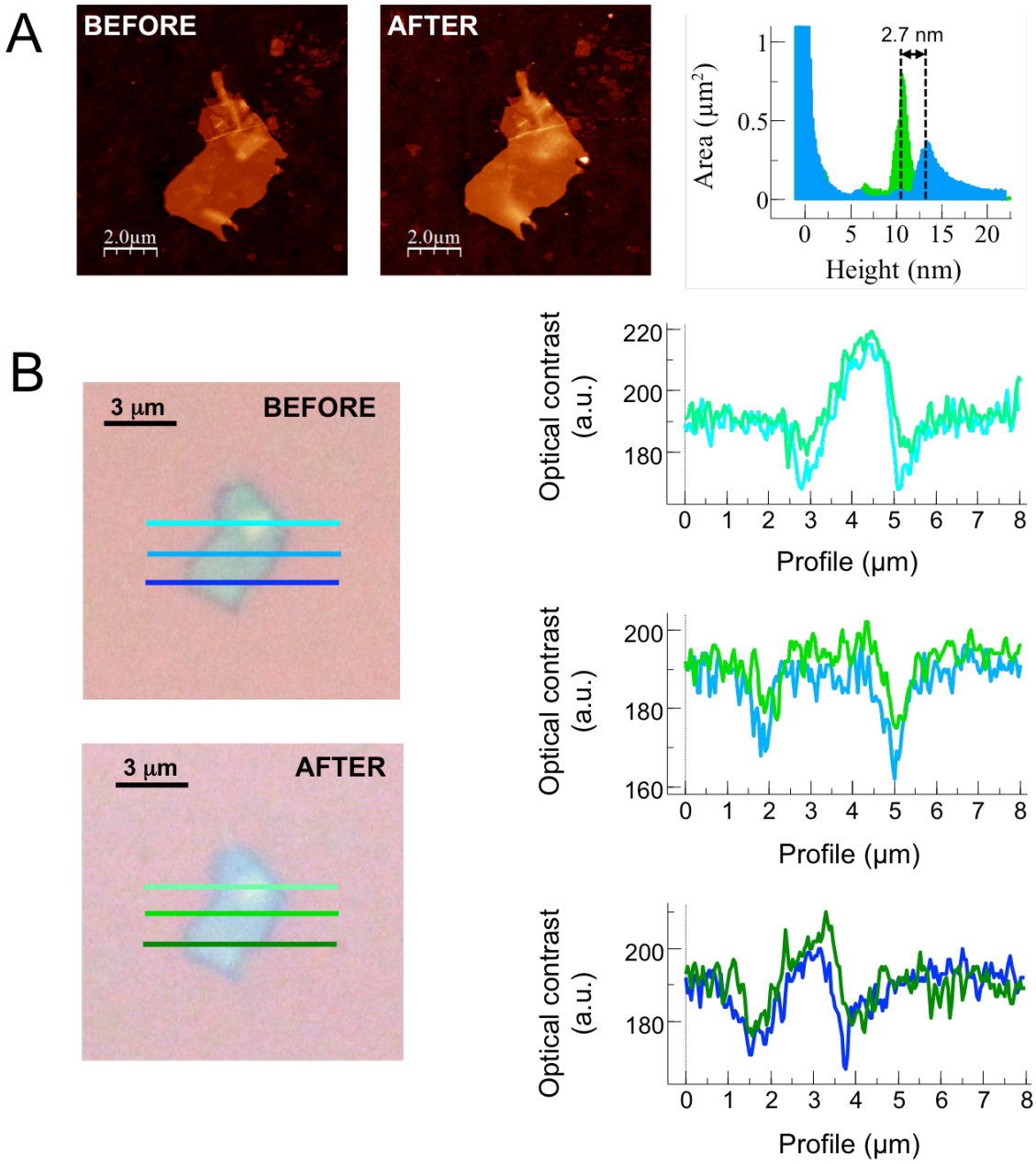

Figure S7. a) Left: AFM images of a few-layer antimonene flake as deposited and after the functionalization with PDI molecules. Right: Height histograms of the flake before (green) and after functionalization (blue), showing an average thickness increase of 2.7 nm. b) Left: different optical images acquired using white light and the corresponding measured optical contrast. Solid lines represent the different analysed profiles.

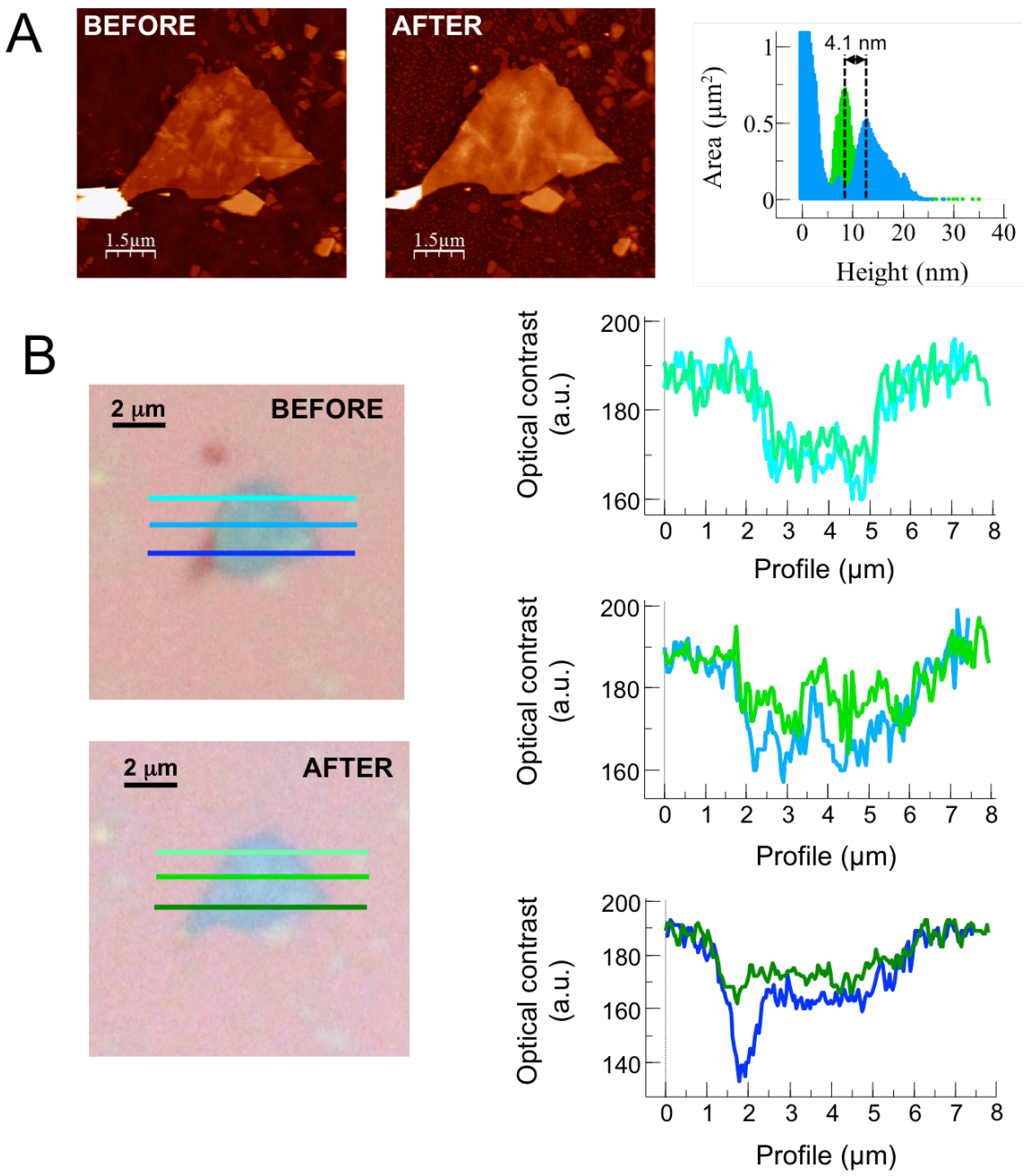

Figure S8. a) Left: AFM images of a few-layer antimonene flake as deposited and after the functionalization with PDI molecules. Right: Height histograms of the flake before (green) and after functionalization (blue), showing an average thickness increase of 4.1 nm. b) Left: different optical images acquired using white light and the corresponding measured optical contrast. Solid lines represent the different analysed profiles.

6. Scanning Raman Microscopy (SRM) of pristine and functionalized few-layer antimonene flakes

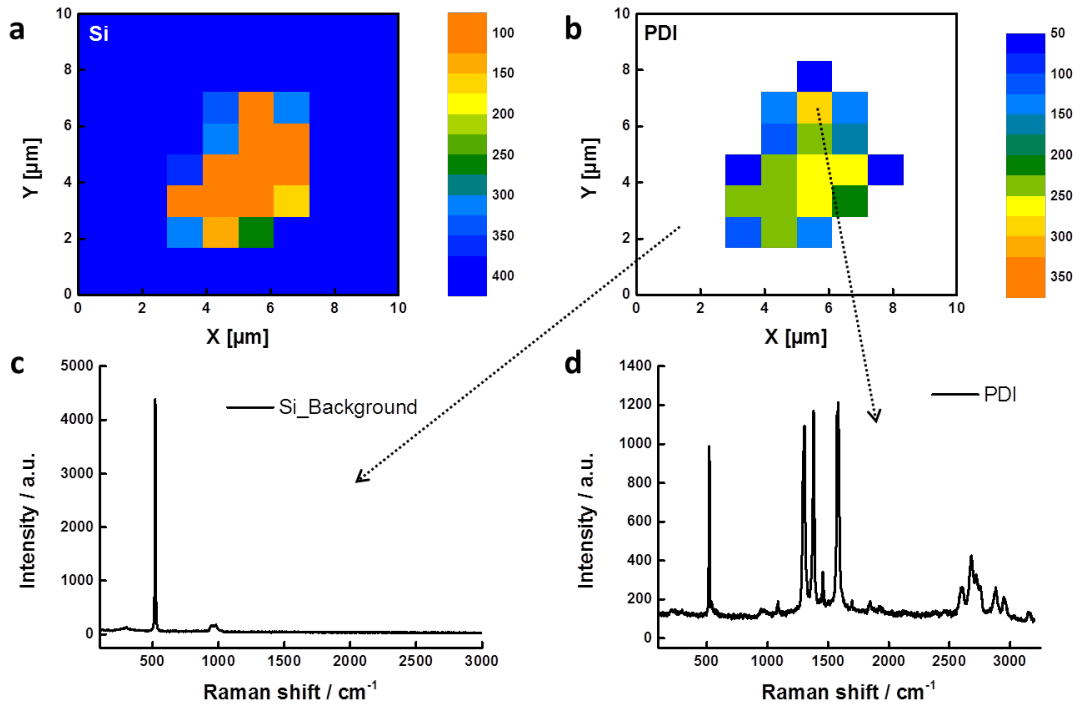

Figure S9. a) Raman mapping displaying the Silicon attenuation as an indirect visualization tool at the position of the few-layer antimonene flake presented in Fig. S1. b) Raman mapping of the same flake after the functionalization with PDI molecules. Now, the legend refers to the averaged intensity of the main PDI Raman band evaluated between 1575 and 1585 cm^{-1}. c) Single Point Raman Spectrum at a position next to the few-layer antimonene flake. Apparently, only the Raman signal of the pure Si/SiO_2 background is present. d) Single Point Raman Spectrum taken on top of the antimonene flake at the position of maximum PDI intensity. Moreover, this plot nicely confirms the self-assembly of PDI molecules solely on top of the few-layer antimonene flakes.

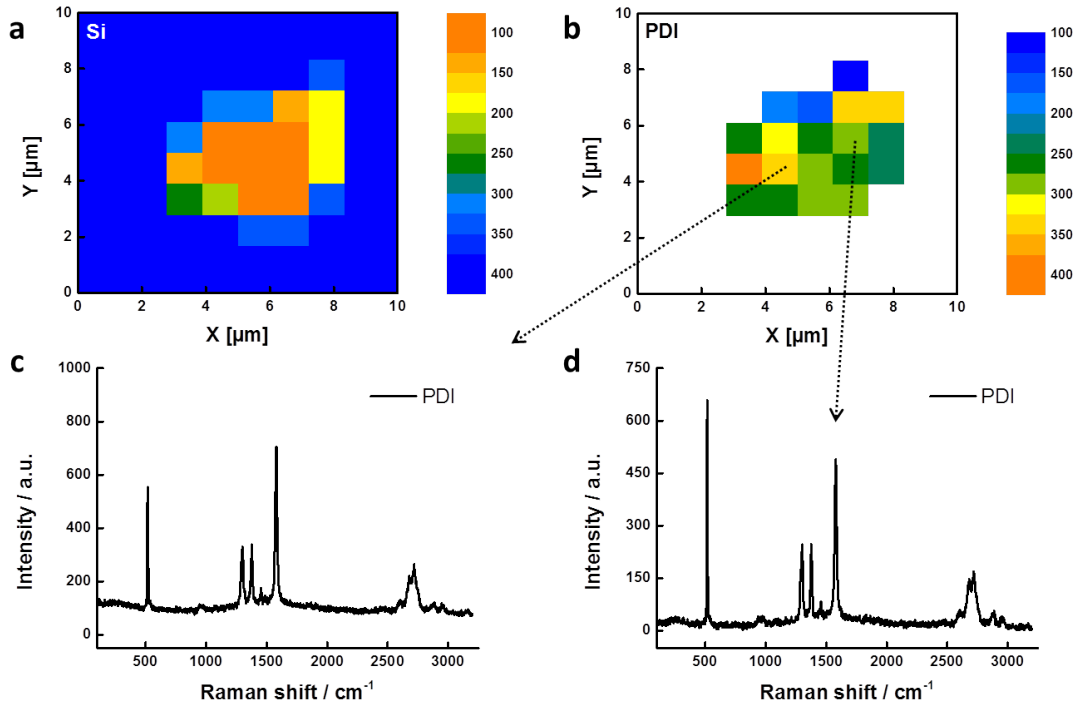

Figure S10. a) Raman mapping displaying the Silicon attenuation as an indirect visualization tool at the position of the few-layer antimonene flake presented in Fig. S2. b) Raman mapping of the same flake after the functionalization with PDI molecules. Now, the legend refers to the averaged intensity of the main PDI Raman band evaluated between 1575 and 1585 cm^{-1}. c) Single Point Raman Spectrum taken in the left part of the antimonene flake. d) Single Point Raman Spectrum taken in the right part of the antimonene flake. Comparison of the both Raman spectra indicates a homogeneous coverage of the sample with PDI molecules.

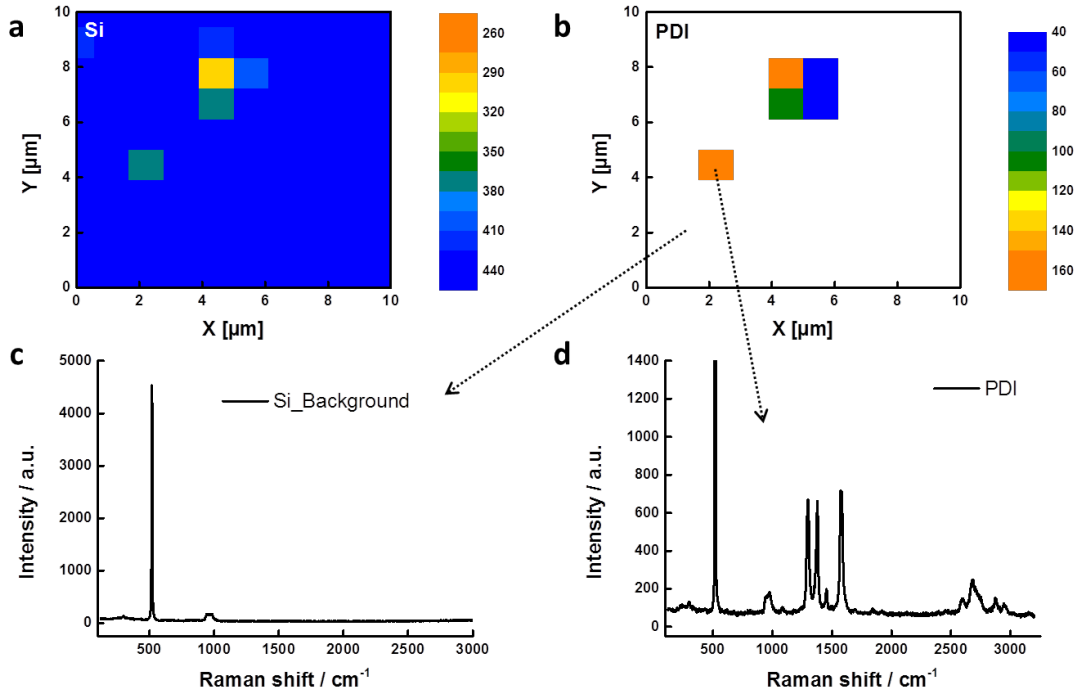

Figure S11. a) Raman mapping displaying the Silicon attenuation as an indirect visualization tool at the position of the few-layer antimonene flakeS presented in Fig. S6. b) Raman mapping of the same area after the functionalization with PDI molecules. Now, the legend refers to the averaged intensity of the main PDI Raman band evaluated between 1575 and 1585 cm^{-1}. c) Single Point Raman Spectrum at a position next to the few-layer antimonene flake. Apparently, only the Raman signal of the pure Si/SiO_2 background is present. d) Single Point Raman Spectrum taken on top of the antimonene flake. Due to the small size of the flake, it can only be represented by one spectrum.

7. Wavelength dependent Raman spectroscopy

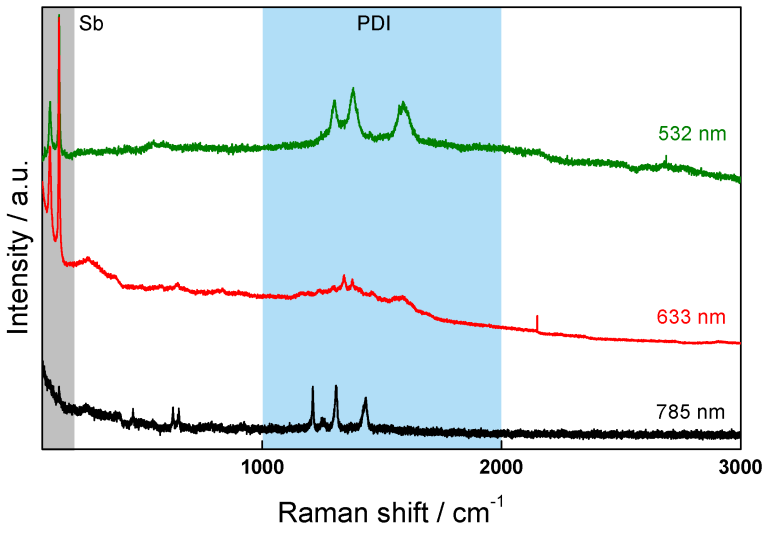

Figure S12. a) Influence of the laser excitation wavelength (532, 633 and 785 nm) on the Raman spectra of bulk FL–Sb functionalized with PDI. The characteristic areas of the Sb and PDI are highlighted with coloured bars.

7. Scanning XPS photoelectron microscopy

Deconvolution of Sb 3d Core Levels

The line shape of Sb 3d core levels was fitted using a Shirley background and asymmetric doublet pseudo-Voigt functions for Sb 3d and a single function for O 1s, which appears in the same binding energy range.[20] The fit was optimized using a Levenberg-Marquardt algorithm with a routine running in IGOR Pro (WaveMatrix Inc.). The quality of the fit was judged from a reliability factor, the normalized χ^2.

Supplementary Table 1: Binding energies (eV, referred to Fermi energy) of the components shown in Fig. 2b and 2d.

Sample	Sb $3d_{5/2}$	Sb $3d_{5/2}$ (oxidized)	O 1s	BE difference Sb $3d_{5/2}$ (oxidized)-Sb $3d_{5/2}$
Reference	528.62	530.88	532.61	2.26
Functionalized	528.62	530.49	532.48	1.87

Fig. S13 shows a summary of Sb 3d core levels taken in different points of the reference sample (Fig. S13c) and of the functionalized sample (Fig. S13d). Note that the intensity ratio between metallic and oxidized Sb components is similar in all the points, as evidenced from the similar line shape of the Sb 3d3/2 components (around 540 eV BE). On the contrary, the intensity of the O 1s peak changes significantly in the different flakes. Note also the case of point E of the functionalized sample, which is dominated by the O 1s line shape.

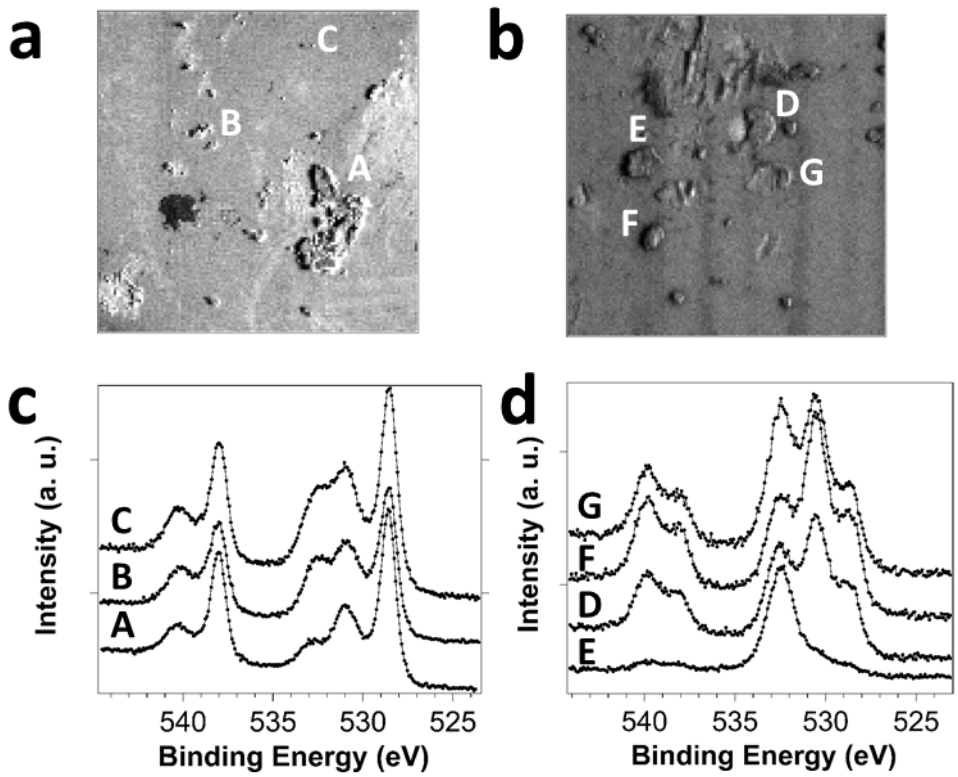

Figure S13. a) and b) Sb 3d images from the reference sample and the functionalized sample, respectively, as described in Fig. 2. c) Sb 3d peak from points A, B and C in the reference sample. The peaks B and C are offset in vertical direction. d) Sb 3d peak from points D, E, F and G in the functionalized sample. The peaks D, F and G are offset in vertical direction and peak E is multiplied by a factor 0.4. In panels c) and d), black dots are experimental points and the lines are a guide to the view.

8. Theoretical calculations

Supplementary Table 2: Structure parameters and k-point setup of BP models

	BP-bulk	BP-ML
a	3.310	3.296
b	4.380	4.591
c	10.581	25.0
k-mesh	19 x 19 x 7	19 x 19 x 1

Optimized cell dimensions of bulk and monolayer BP (in Å). The unit cell is orthorhombic and contains 8 atoms. The experimental parameters of bulk BP are (in Å): a = 3.3136, b = 4.3863, c = 10.478 (values from the CRC Handbook[18]).

Supplementary Table 3: Structure parameters and k-point setup of Sb models

	Sb-bulk	Sb-ML	Sb-DL
a	4.360	4.115	4.242
b	4.360	4.115	4.242
c	11.221	26.8	25.7
k-mesh	19 x 19 x 7	19 x 19 x 1	19 x 19 x1

Optimized cell dimensions of bulk, monolayer and double layer Sb (in Å). The unit cell used for the computation is hexagonal and contains 6 atoms. The experimental parameters of Sb are (in Å): a = b = 4.308, c = 11.274 (values from the CRC Handbook[18] converted to hexagonal setup).

Supplementary Table 4: Structure parameters and k-point setup of PDI on a BP monolayer or Sb mono/double layer, respectively

substrate	BP-ML	Sb-ML	Sb-DL
a	19.776	20.573	21.209
b	22.956	20.573	21.209
c	25.0	26.8	30.0
distance PDI-BP (opt.)	3.3	3.4	3.6
k-mesh	3 x 3 x 1	4 x 4 x1	4 x 4 x 1

Setup for PDI adsorbed on BP/Sb mono/double layers. Note, that in case of BP the cell is orthorhombic, in case of Sb it is hexagonal.

The dramatic quenching of the photoluminiscence strongly indicates that the PDI molecules are adsorbed with the perylene core lying flat on the substrate, similar to other 2D materials like graphene, at least at lower coverage.[21] Consequently, we only considered a PDI coverage in our DFT calculations, where perpendicular adsorption can be excluded. To make sure that the experimentally attached side chains to the PDI core do not change this picture, we have implemented some DFT calculations focused on the interaction of the periphery of the molecules with the antimonene surface. As the full molecule would not be feasible within reasonable computing time, we decided to model half of the molecules, *i.e.* cutting through the PDI core (and saturating dangling bonds with hydrogen). Although we chose start geometries where the (halved) perylene core was not parallel with respect to the antimonene surface, it accommodated again a parallel orientation during geometry optimization. Moreover, the protecting tert-butyl moieties also interact via van der Waals forces with the substrate. This confirms that the periphery is not forcing the PDI molecules to lie perpendicular to the antimonene. The adsorption energy corresponding to Fig. S14 is calculated as -1.13 eV (vdW contribution is -1.23 eV).

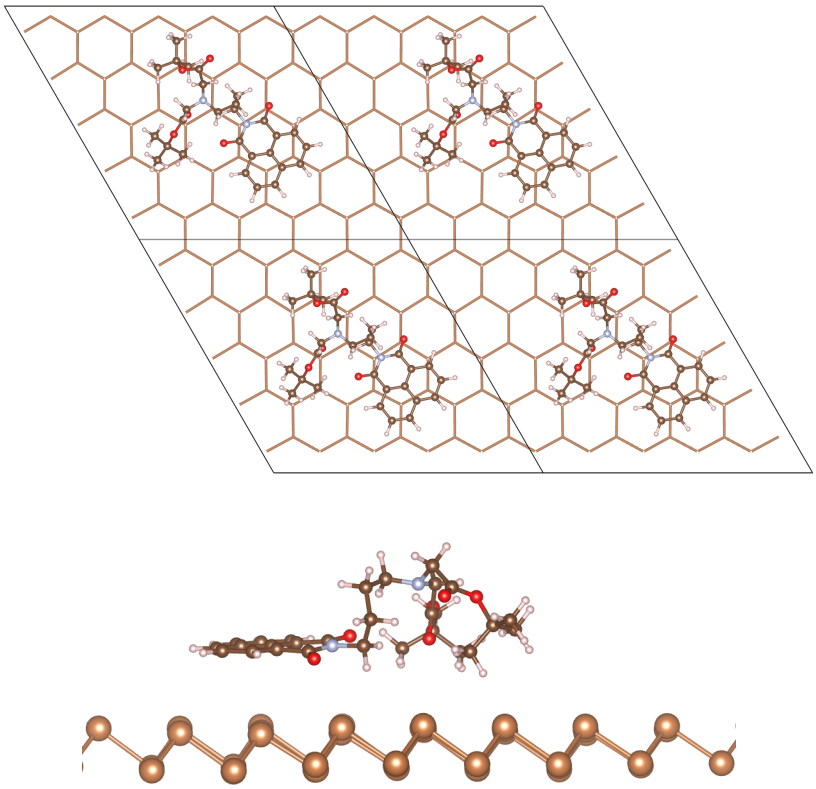

Figure S14. Optimized adsorption geometry of a half PDI core with peripheral side chain R1 (see Fig. 1a in paper) on antimonene (top view and side view, respectively).

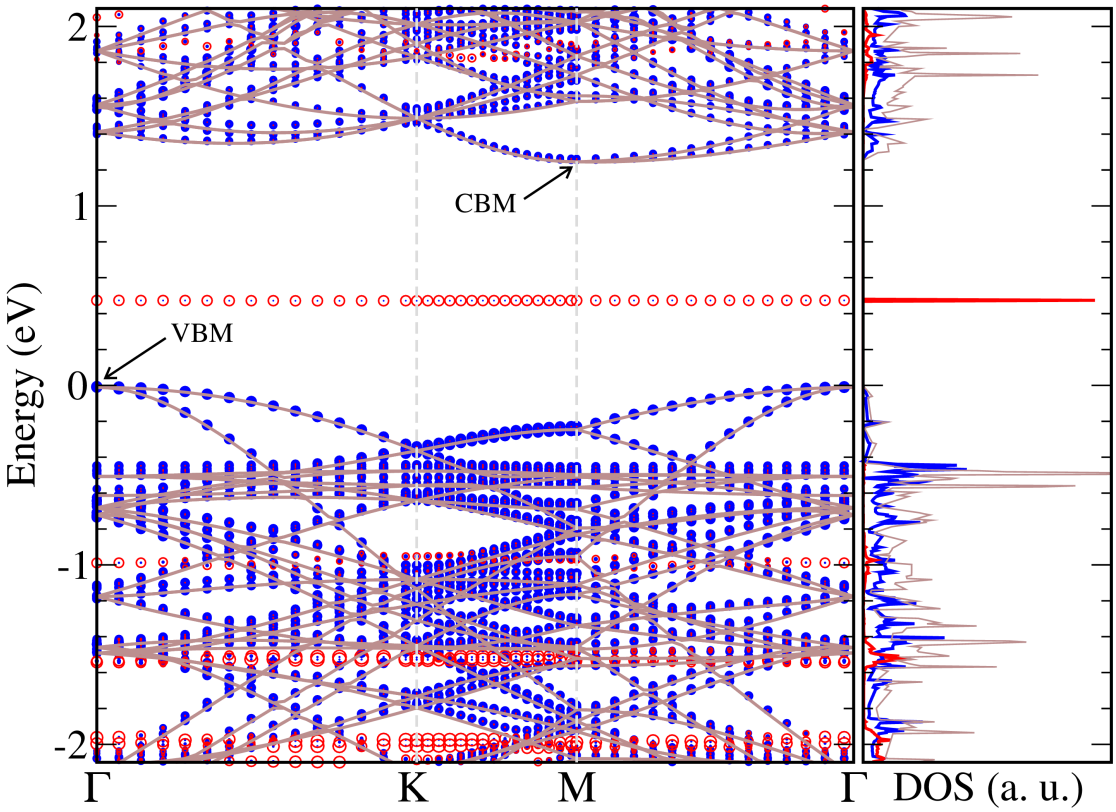

Figure S15. Band structures and density of states of PDI@Sb-ML. PBE-D3 Band structures and density of states (DOS) of a pristine Sb monolayer (grey), and the PDI-adsorbed Sb monolayer (blue and red). Blue dots/lines and red circles/lines indicate Sb and PDI contributions in the band structure/DOS, respectively. The valence band maximum (VBM) and conductance band minimum (CBM) of the Sb monolayer are indicated.

9. Temperature dependent Raman spectroscopy

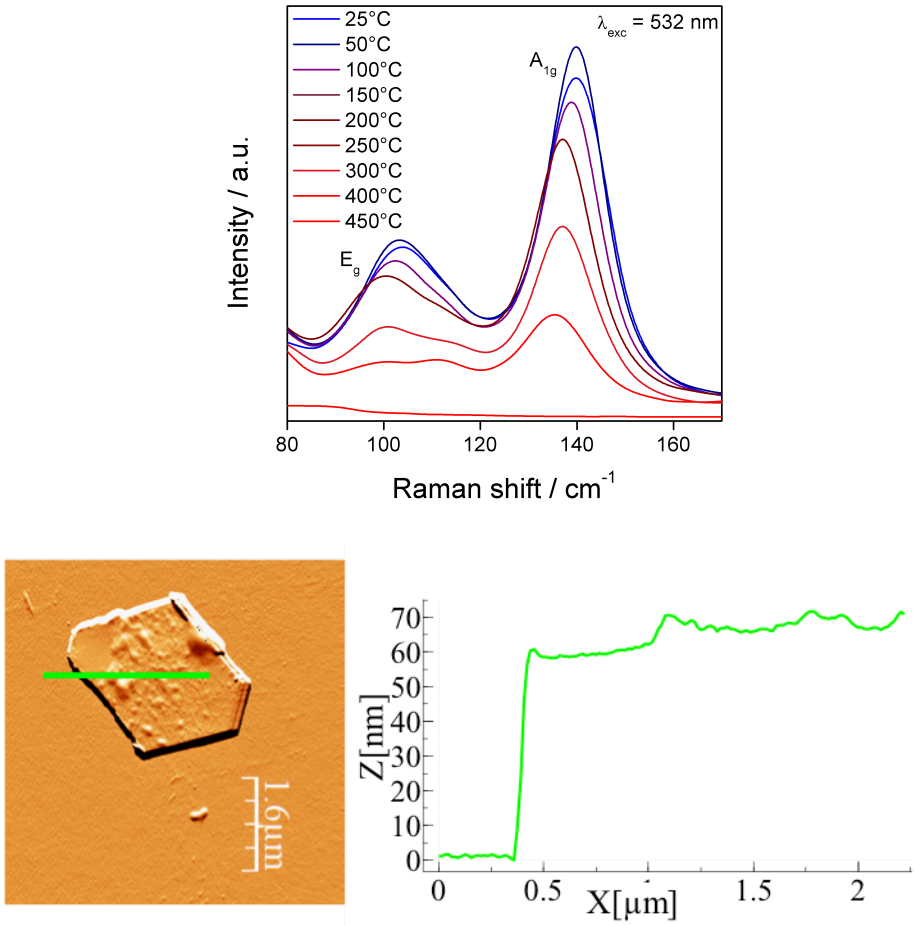

Figure S16. Temperature-dependent statistical Raman spectroscopy (TSRS) of an antimonene flake of *ca*. 60 nm thick in the temperature region between 25 and 450 °C. Remarkably, the sample is stable until ca. 400 ºC, being completely degraded at 450 ºC.

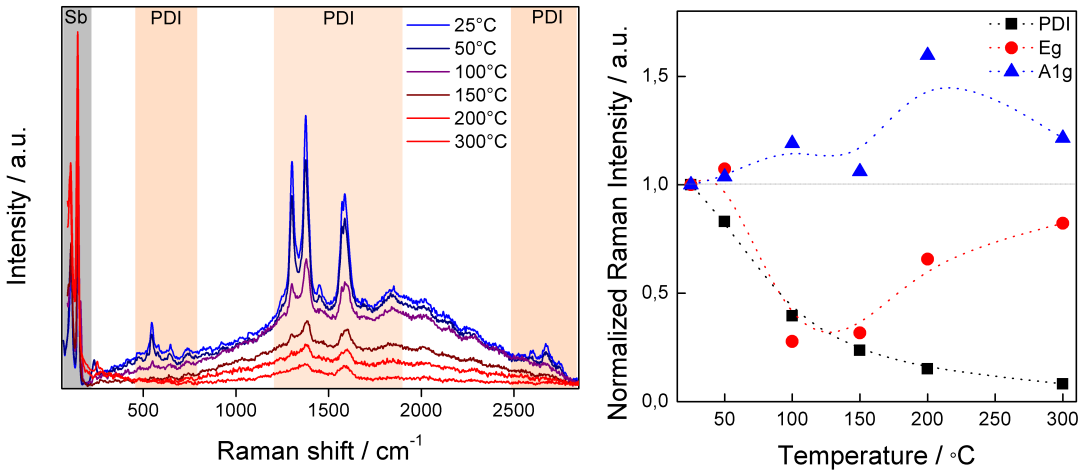

Figure S17. Left: Temperature-dependent statistical Raman spectroscopy (TSRS) of an antimonene flake of *ca*. 60 nm thick deposited on a gold substrate in the temperature region between 25 and 300 °C. The desorption of the PDI molecules is reflected in a concomitant decrease of the characteristic PDI peaks intensity, as well as a progressive increase of the fluorescence background, until its complete disappearance at *ca*. 300 ºC, in excellent accordance with the AFM results (see next section). Right: Evolution of the normalized Raman intensities of the antimonene E_g and A_{1g} modes and the PDI ν_{Ag} with the temperature.

10. Thermal desorption characterized by AFM microscopy

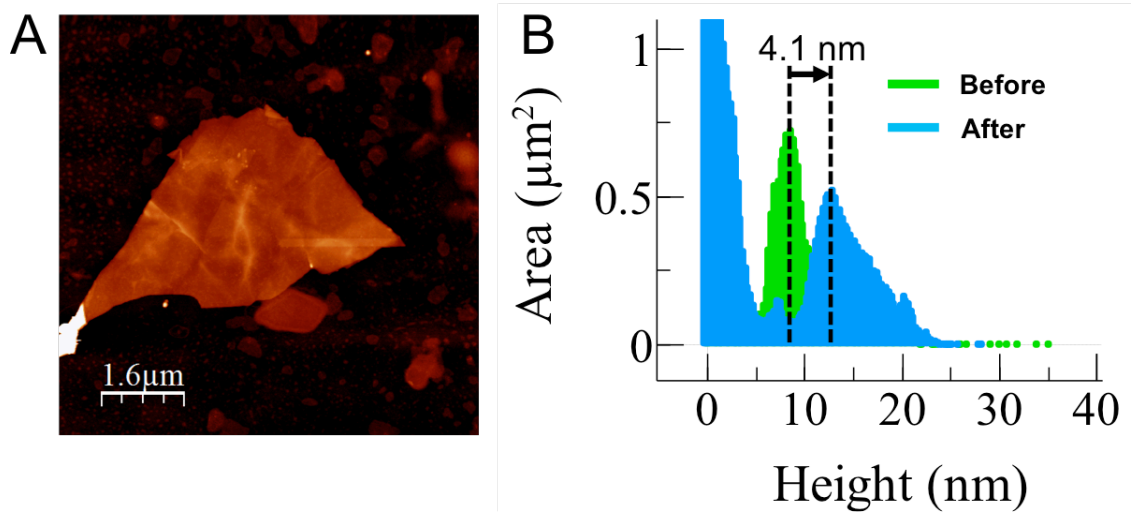

Figure S18. a) AFM image of a few-layer antimonene flake shown in Fig 4 of the main text before functionalization. b) Height histograms of the flake before (green) and after functionalization (blue), showing an average thickness increase of 4.1 nm. For the sake of clarity, the substrate peak has been cut to 1.1 μm^2.

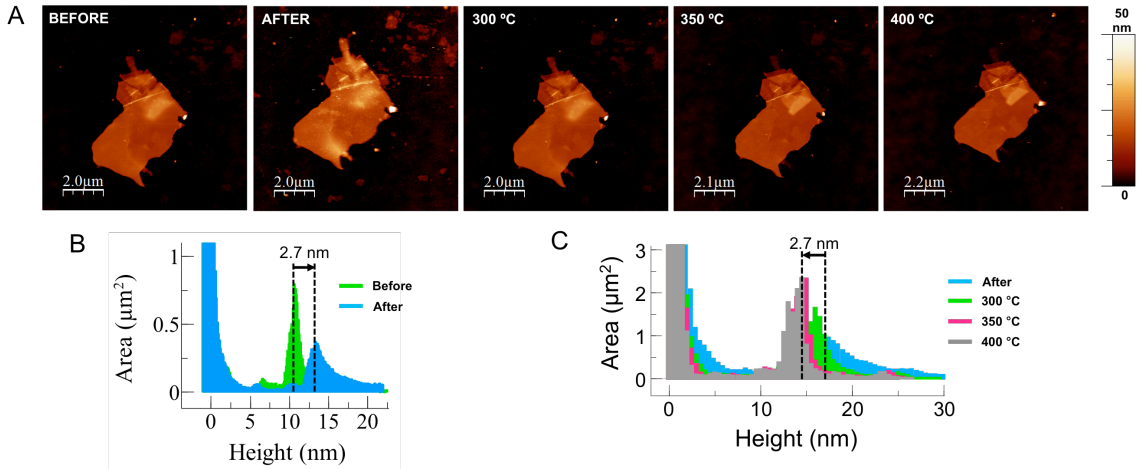

Figure S19. a) Thermal desorption of the PDI adlayer from the antimonene surface characterized by means of AFM topography images measured after heating at different temperatures, and the corresponding histograms showing the decrease in the thickness of the PDI organic layer (2.7 nm). After heating at 400 ºC the original value of the pristine flake was recovered, confirming the complete thermal removal of the PDI.

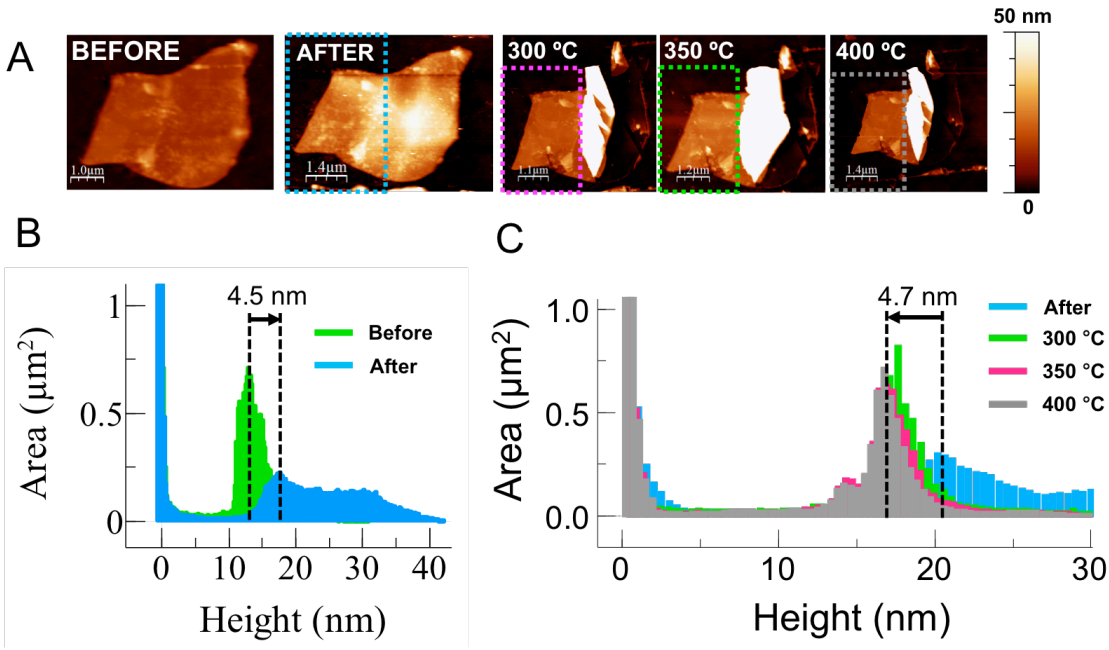

Figure S20. a) Thermal desorption of the PDI adlayer from the antimonene surface characterized by means of AFM topography images measured after heating at different temperatures, and the corresponding histograms showing the decrease in the thickness of the PDI organic layer (4.5 nm). After heating at 400 ºC the original value of the pristine flake was recovered, confirming the complete thermal removal of the PDI. It is worth to remark here that the flake suffered a folding during the heating process, which is reflected in the brighter areas of the AFM images. Histograms in c) were obtained from the unfolded area of the flake.

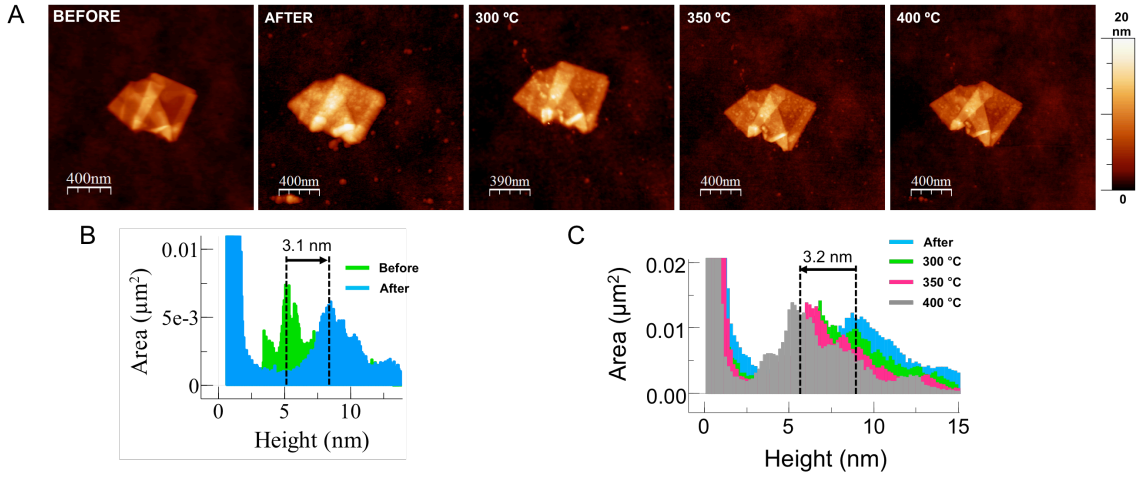

Figure S21. a) Thermal desorption of the PDI adlayer from the antimonene surface characterized by means of AFM topography images measured after heating at different temperatures, and the corresponding histograms showing the decrease in the thickness of the PDI organic layer (3.1 nm). After heating at 400 ºC the original value of the pristine flake was recovered, confirming the complete thermal removal of the PDI.

11. Non-covalent functionalization of liquid phase exfoliated samples

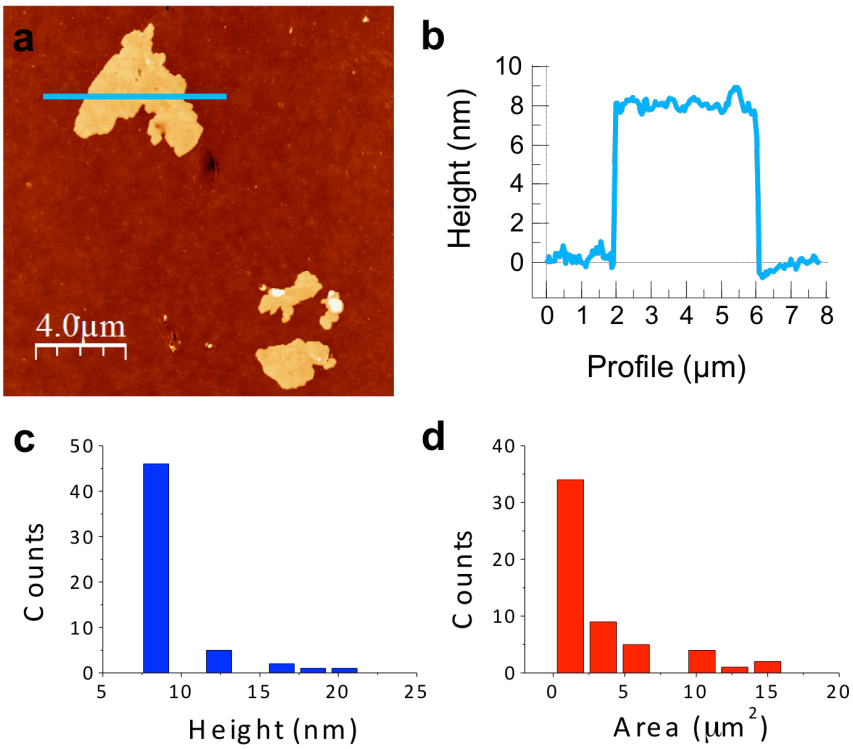

Figure S22. a) AFM topographic analysis of LPE few-layer antimonene flakes drop-casted on SiO_2 from IPA suspensions. a) Representative topographic image showing several flakes. b) Profile along the horizontal line in a). c) Height histogram from a set of 12 images comprising a total of 55 flakes. The histogram shows a marked peak for flakes' height ~ 8 nm. d) Area histogram from the same set of images as in c). Most of the flakes had surface areas below 5 μm^2.

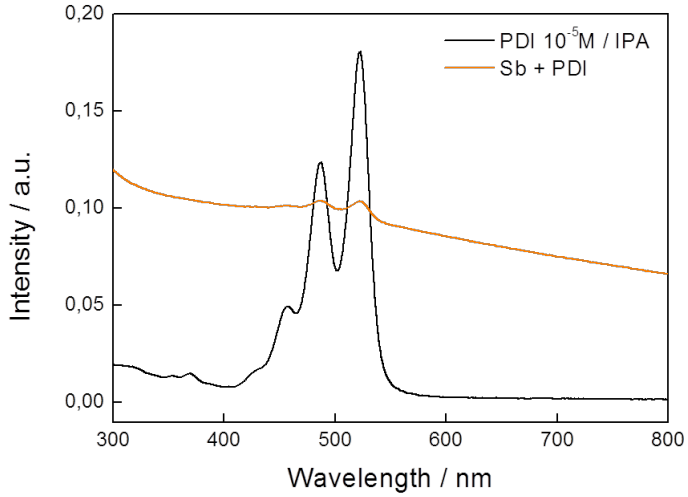

Figure S23. UV/Vis spectra of PDI 10^{-5} M in IPA and the corresponding Sb-PDI hybrid re-dispersed in IPA after centrifugation at 15000 rpm for 10 min.

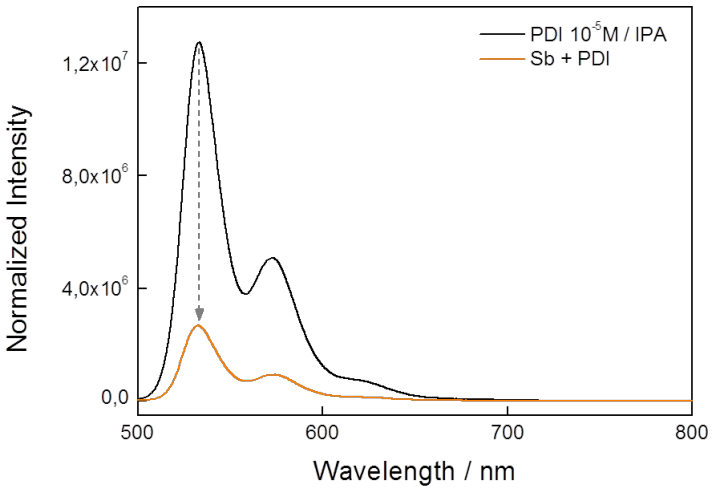

Figure S24. Fluorescence emission spectra of PDI 10^{-5} M and the Sb-PDI hybrid re-dispersed in IPA after centrifugation at 15000 rpm for 10 min; λ_{exc}=455 nm.

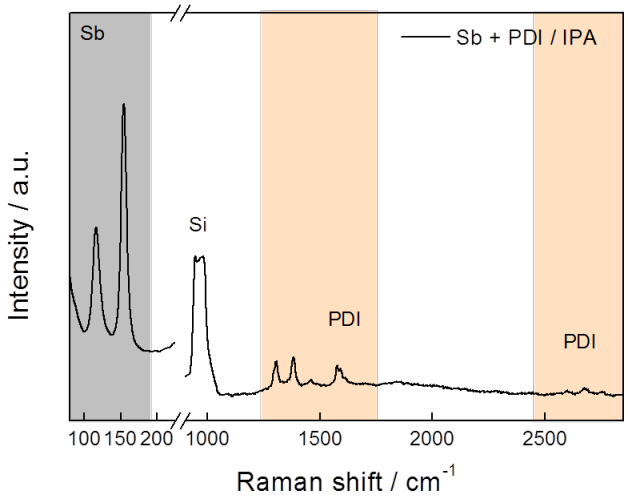

Figure S25. Raman spectra (excitation at 532 nm) of a representative Sb-PDI flake showing both the antimonene and PDI Raman bands.

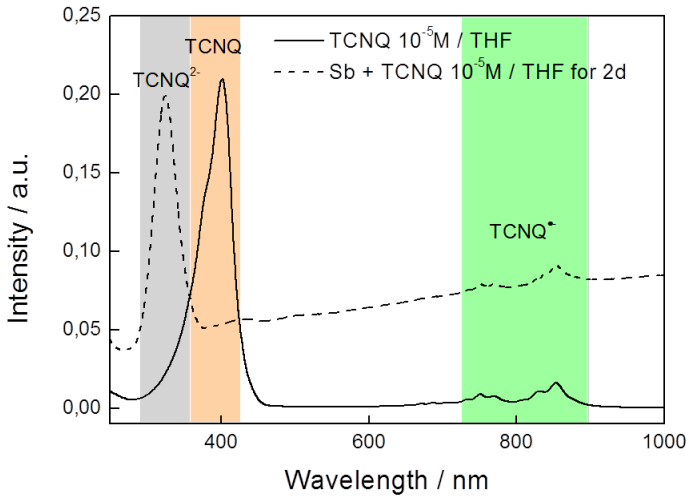

Figure S26. Electronic absorption spectra of a 10^{-5} M TCNQ solution in THF and the corresponding Sb-TCNQ hybrid measured under inert conditions, highlighting the formation of $TCNQ^{2-}$. The electronic absorption spectra fingerprints of the different TCNQ species are indicated with coloured bars.

References

[1] P. Ares, F. Aguilar-Galindo, D. Rodríguez-San-Miguel, D. A. Aldave, S. Díaz-Tendero, M. Alcamí, F. Martín, J. Gómez-Herrero, F. Zamora, *Adv. Mater.* 2016, *28*, 6332–6336.

[2] A. Gimeno, P. Ares, I. Horcas, A. Gil, J. M. Gómez-Rodríguez, J. Colchero, J. Gómez-Herrero, *Bioinformatics* 2015, btv278.

[3] I. Horcas, R. Fernández, J. M. Gómez-Rodríguez, J. Colchero, J. Gómez-Herrero, A. M. Baro, *Rev. Sci. Instrum.* 2007, *78*, 013705.

[4] M. K. Abyaneh, L. Gregoratti, M. Amati, M. Dalmiglio, M. Kiskinova, *E-J. Surf. Sci. Nanotechnol.* 2011, *9*, 158–162.

[5] *Rev. Sci. Instrum.* 2003, *75*, 64–68.

[6] G. Kresse, J. Furthmüller, *Comput. Mater. Sci.* 1996, *6*, 15–50.

[7] G. Kresse, J. Furthmüller, *Phys. Rev. B* 1996, *54*, 11169–11186.

[8] G. Kresse, D. Joubert, *Phys. Rev. B* 1999, *59*, 1758–1775.

[9] P. E. Blöchl, *Phys. Rev. B* 1994, *50*, 17953–17979.

[10] J. P. Perdew, K. Burke, M. Ernzerhof, *Phys. Rev. Lett.* 1996, *77*, 3865–3868.

[11] S. Grimme, J. Antony, S. Ehrlich, H. Krieg, *J. Chem. Phys.* 2010, *132*, 154104.

[12] S. Grimme, S. Ehrlich, L. Goerigk, *J. Comput. Chem.* 2011, *32*, 1456–1465.

[13] T. Bučko, J. Hafner, J. G. Ángyán, *J. Chem. Phys.* 2005, *122*, 124508.

[14] M. Methfessel, A. T. Paxton, *Phys. Rev. B* 1989, *40*, 3616–3621.

[15] H. J. Monkhorst, J. D. Pack, *Phys. Rev. B* 1976, *13*, 5188–5192.

[16] *J. Chem. Phys.* 2006, *125*, 224106.

[17] P. E. Blöchl, O. Jepsen, O. K. Andersen, *Phys. Rev. B* 1994, *49*, 16223–16233.

[18] H. W. King, *CRC Handb. Chem. Phys.* 2012, *93*.

[19] M. Marcia, P. Singh, F. Hauke, M. Maggini, A. Hirsch, *Org. Biomol. Chem.* 2014, *12*, 7045.

[20] M. Schmid, H.-P. Steinrück, J. M. Gottfried, *Surf. Interface Anal.* 2014, *46*, 505–511.

[21] N. C. Berger, S. Winters, C. Backes, C. Yim, K. C. Dümbgen, I. Kaminska, S. Mackowski, A. A. Cafolla, A. Hirsch, G. S. Duesberg, *Nanoscale*, 2015, *7*, 16337–16342